THE JOURNAL OF PHYSICAL CHEMISTRY C

Article

pubs.acs.org/JPCC

Mechanism of the Key Impact of Residual Carbon Content on the Reliability of Integrated Resistive Random Access Memory Arrays

Gang Niu,*[,†,‡] Xavier Cartoixà,[§] Alessandro Grossi,[∥] Cristian Zambelli,[∥] Piero Olivo,[∥] Eduardo Perez,[‡] Markus Andreas Schubert,[‡] Peter Zaumseil,[‡] Ioan Costina,[‡] Thomas Schroeder,[‡,⊥] and Christian Wenger*[,‡]

[†]Electronic Materials Research Laboratory, Key Laboratory of the Ministry of Education & International Center for Dielectric Research, Xi'an Jiaotong University, Xi'an 710049, China

[‡]IHP GmbH, Im Technologiepark 25, 15236 Frankfurt (Oder), Germany

[§]Departament d'Enginyeria Electrònica, Universitat Autònoma de Barcelona, 08193 Bellaterra, Spain

[∥]Dip. di Ingegneria, Università degli Studi di Ferrara, Via Saragat 1, Ferrara 44122, Italy

[⊥]Brandenburgische Technische Universität, Konrad-Zuse-Strasse 1, 03046 Cottbus, Germany

Supporting Information

ABSTRACT: Resistive random access memories (RRAM) require high density, low power consumption and high reliability. Systematic statistic electrical, material and theoretical studies were demonstrated in this work to point out and clarify a key impact of carbon residues on the resistive switching (RS), particularly the endurance, of the integrated HfO_2-based 4 kbit RRAM array. The mechanism of the carbon atoms interacting with oxygen vacancies and serving also as filament was understood in nanoscale by performing density functional theory (DFT) calculations. Under an oxygen-deficient environment, carbon atoms tend to fill in oxygen vacancy ($V_O^{\cdot\cdot}$) sites and could form conductive filaments which require higher energy to be broken compared to the original $V_O^{\cdot\cdot}$ filaments. By controlling the residual carbon concentration lower than 4%, highly reliable HfO_2-based integrated 4 kbit RRAM array was achieved, which is of great interest for future nonvolatile memories.

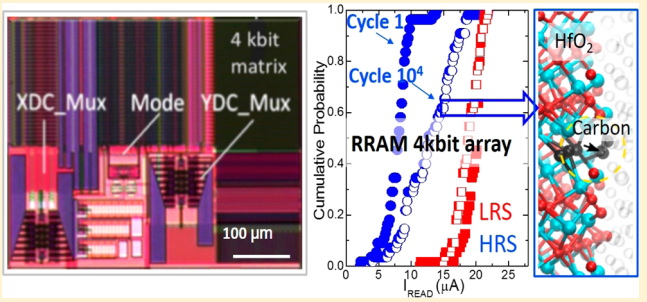

1. INTRODUCTION

The requirement of novel memories with high density and nonvolatile data storage has recently driven international industries and academic communities to search for new materials and concepts.[1−6] HfO_2-based resistive random access memories (RRAM) represent one of the most promising candidates to satisfy the multiple needs. Compared to other counterparts, HfO_2-based RRAM demonstrates compatibility with modern complementary metal oxide semiconductor (CMOS) processing,[7] fast and low power switching,[8] high endurance,[9] and excellent scaling capability down to 10 nm.[10]

RRAM devices are generally composed of a metal−insulator−metal (MIM) structure. The resistive switching (RS) occurs either at the insulating oxide/metal interfaces or relies on the filamentary ion migration in the oxide film bulk, the latter of which does not depend on the device area thus being more suitable for device scalability.[11] In filament-type RRAM, a conductive filament (CF) consisting of oxygen vacancies ($V_O^{\cdot\cdot}$) or excess metal cations is established after an electroforming process, due to the activation of the ion migration induced by a local Joule heating effect.[12,13] The RS relies subsequently on the rupture of the CF typically at one of the metal/oxide interfaces (Reset or high resistance state, HRS) and the reformation of a continuous CF in the oxide film bulk (set or low resistance state, LRS), by applying an opposite or a same bias with the electroforming operation, respectively. The failure of the devices is related to the presence of an inflexible CF in oxide films, i.e., a hard breakdown of the devices. The further improvement of RRAM device performances including the reliability, consists therefore in understanding and controlling filament-related materials issues, such as crystallinity, carbon contaminations, doping etc. However, it is not a trivial task to correlate each material property to electrical performances of the RRAM devices, particularly of the integrated 1-transistor-1-resistor (1T1R) devices, as different types of materials modification appear often simultaneously, e.g., elements doping into HfO_2 usually change its recrystallization temperature.[14,15] In addition, in order to unambiguously clarify material effects on scaled device performances, a statistic electrical study in pulse mode, which is the operation mode of final high-end applications of RRAM devices, directly on integrated 1T1R RRAM arrays is highly required. Moreover, to

Received: December 20, 2016
Revised: March 1, 2017
Published: March 6, 2017

DOI: 10.1021/acs.jpcc.6b12771
J. Phys. Chem. C XXXX, XXX, XXX−XXX

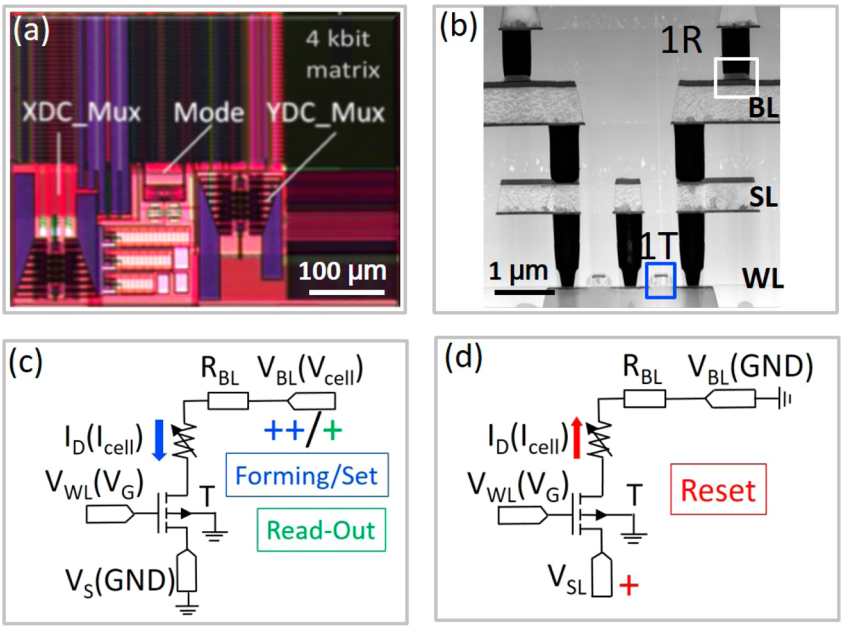

Figure 1. (a) Photo of 4kbit memory array with control circuits. XDC_Mux, YDC_Mux, and Mode denote the word address decoder, the bit address decoder, and the operation control circuit, respectively. (b) TEM cross-sectional image of 1T1R architecture with a NMOS access transistor (1T, marked by a blue square) and a 0.8 × 0.8 μm^2 MIM cell (1R, marked by a white square); BL, SL, and WL denote the positions of bit line, source line, and word line, respectively. Equivalent circuits of devices operating in (c) forming/set or readout and (d) reset modes. The used terminals are shown, and the arrows demonstrate the current directions. V_{BL}, V_{cell}, V_{WL}, V_G, and V_S represent BL, cell, WL, gate, and source voltages, respectively; R_{BL} denotes BL resistance; and I_D, and I_{cell} denote drain and cell currents, respectively. GND means ground and T represents the transistor.

understand the physical mechanism of the materials impacts in nm scale, theoretical calculations are indispensable as well. In particular, residual impurities like carbon in HfO_2 films are considered as significant factors strongly influencing the electrical performances of HfO_2-based solid state devices, including metal-oxides-semiconductor (MOS) and MIM devices.[16−20] For instance, Miao et al.[18] experimentally reported that carbon impurities aggravate interface properties and increase bulk defect density in HfO_2, which results in the degradation of barrier heights and poor performance of the high-k MIM capacitors. Choi et al.[20] theoretically pointed out that carbon introduces charge-state transition levels near the semiconductor conduction-band edges, leading to border traps and/or leakage current in HfO_2-based MOS devices. Our group has studied the carbon effects on performances of HfO_2-RRAM devices and preliminary results indicate that, carbon atoms dynamically segregate to the Ti/HfO_2 interface under RS[19] and the reduction of carbon concentration by increasing deposition temperature to 300 °C in atomic layer depostion (ALD) grown HfO_2 1T1R RRAM devices leads to better device performances including power consumption and endurance.[21] However, these works are all based on electrical measurements in direct current (dc) mode on large size (mm-size) devices or single devices. Studies directly on the RRAM memory array by statistic measurements in pulse mode, which is used in final high-end RRAM applications to operate devices, are still lacking. More importantly, the mechanism of the impact of residual carbon on the reliability of the RRAM array and physical insights into the interaction between carbon atoms and $V_O^{\cdot\cdot}$ based CFs, which is responsible for RS, need to be clarified.

Here in this work we report an in-depth study on HfO_2-based integrated 1T1R RRAM 4kbit arrays with the combination of statistic electrical measurements in pulse mode and a systematic materials characterization. With the help of theoretical ab initio density functional theory (DFT) calculations, the key impact of carbon residues on the reliability of RRAM devices is highlighted and thoroughly understood. Highly reliable HfO_2 RRAM arrays have been realized by reducing the residual carbon concentration.

2. EXPERIMENTAL SECTION

A standard 0.25 μm CMOS process line was employed. Figure 1 illustrates the final structure of the device. First, the NMOS transistors were processed, with a width (W) of 1.14 μm and length (L) of 0.24 μm. The RS cell was then placed between the metallization levels 2 and 3. In order to reduce the surface roughness of the bottom electrode, a 20 nm thick TiN layer was additionally deposited by atomic vapor deposition (AVD). Ten nm HfO_2 films were grown at 320 and 400 °C in the same AVD chamber using liquid metal organic TEMAH (tetrakis (ethylmethylamino)hafnium, $Hf[N(CH_3)(C_2H_5)]_4$) precursor.[22] Finally, HfO_2 was capped by 7 nm ionized metal plasma (IMP) Ti and 150 nm TiN grown by physical vapor deposition (PVD).[23] The ∼20 nm HfO_2 thin films on TiN/Si (001) templates for material characterizations were fabricated in the same AVD system at 320 and 400 °C. The electrical properties of the memory cells were measured in a Cascade PA200 Semiautomatic Probe System and the current−voltage (I−V) curves were collected by using a Rifle SE equipment. The crystalline properties of the HfO_2 films were macroscopically examined by grazing incident X-ray diffraction (GIXRD) by employing a Rigaku Smartlab diffractometer with a 9 kW rotating anode (Cu Kα1, λ = 1.5406 Å). High resolution transmission electron microscopy (HRTEM) measurements were performed using the FEI TITAN 80-300 Berlin Holography system operated at 300 kV. The sample lamellas

DOI: 10.1021/acs.jpcc.6b12771
J. Phys. Chem. C XXXX, XXX, XXX−XXX

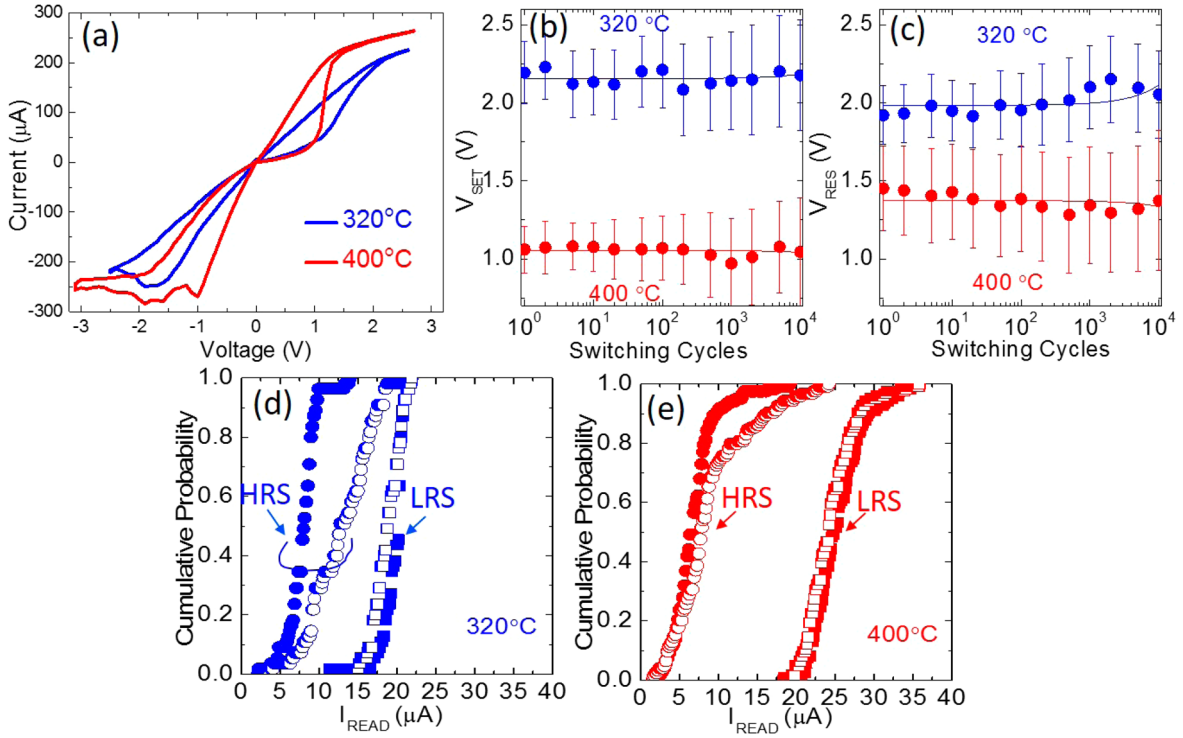

Figure 2. Electrical measurements on arrays with HfO_2 films deposited at 320 °C (blue curves) and 400 °C (red curves): (a) $I-V$ curves in dc mode; plotting of (b) set voltage V_{SET} and (c) reset voltage V_{RES}, as a function of switching cycles. Cumulative probability of the LRS and HRS current values after 1 (closed symbols) and 10^4 cycles (open symbols) for (d) 320 °C devices and (e) 400 °C devices.

were prepared by conventional mechanical polishing and Ar ion milling. The film thicknesses were also determined by TEM measurements. The atomic concentration of residual carbon in the HfO_2 films was characterized by both sputtering X-ray photoelectron spectroscopy (XPS) with Al Kα excitation energy (1486.6 eV) using a PHI Versa Probe II Scanning XPS Microprobe system and time-of-flight secondary ion mass spectrometry (Tof-SIMS) using an IONTOF TOF-SIMS 5 equipment with an Cs sputtering beam (1 keV) and a Bi_1 analysis beam (25 keV). Theoretical calculations were made within density functional theory (DFT), as implemented in the SIESTA package. We used norm-conserving pseudopotentials for the core electrons and a double-ζ plus polarization (DZP) basis set for the valence electrons, which is necessary in order to obtain values for the defect formation energies in quantitative agreement with those obtained with plane wave codes. The exchange-correlation energy is calculated within the generalized gradient approximation (GGA) in the parametrization of Perdew–Burke–Ernzerhof.[24] In order to minimize the coupling between the single impurity/filament instances, which we take to be along the c axis for the crystalline material (see ref 25 for the definition of the axes), we use a $3 \times 3 \times 4$ supercell of the monoclinic unit cell, sampling the Brillouin zone with a grid of $2 \times 2 \times 1$ **k** points chosen according to the Monkhorst–Pack algorithm.[26] All the structures discussed have been relaxed until all the forces on the atoms were lower than 0.04 eV/Å. Formation/process energies are computed as the difference in total internal energies of the final state minus the initial state, $E_{form} = E_{final} - E_{initial}$. When studying charged impurities the computational supercell should have a finite net charge, which is dealt with using a compensating background to achieve overall charge neutrality.[27,28] In such calculations, the presence of the image charges and the compensating background introduces a spurious electrostatic contribution to the total energy that must be subtracted. In a cubic bulk, a Madelung energy is computed in order to remove the leading order contribution.[28] However, low symmetry systems feature a dielectric tensor rather than a constant, plus a noncubic underlying Bravais lattice, preventing the straightforward use of the Madelung correction. We have recently generalized[29] the Madelung correction to the case of an arbitrary static dielectric tensor $\bar{\bar{\varepsilon}}$ and lattice, which we used here.

3. RESULTS AND DISCUSSION

Figure 1a depicts a photograph of tested array architecture with (1) 4kbit memory array 1T1R devices, (2) a word address decoder (gate of the access transistor, XDC MUX), (3) a bit address decoder (YDC MUX), and (4) an operation control circuit (Mode). The 6-in/2^6-out row (XDC MUX) and column (YDC MUX) decoders select a single (out of 26) word line (WL) and a single (out of 26) bit/source line (BL/SL) of the memory array, respectively. The drain of the transistor is connected to the bottom metal electrode of the MIM cell at each storage location, as revealed in Figure 1b–d.[30] Figure 1b shows a transmission electron microscopy (TEM) image of a 0.8×0.8 μm^2 MIM cell with 1T1R architecture; in addition an NMOS access transistor featuring $W = 1.14$ μm and $L = 0.24$ μm and the WL, SL, and BL are also shown. Figure 1c and d displays the equivalent circuits of devices operating in forming/set/read-out and reset modes, respectively. In forming/set and read-out modes, voltages are applied to BL (V_{BL}) and the cell current (I_{cell}) flows from R_{BL} to the drain of the transistor. While in reset mode, a voltage is applied to SL (V_{SL}) and I_{cell} flows from transistor drain to R_{BL}. It is noted here that the forming process can be accelerated by selecting multiple rows and/or columns simultaneously. The forming process can be

DOI: 10.1021/acs.jpcc.6b12771
J. Phys. Chem. C XXXX, XXX, XXX–XXX

considered as a soft breakdown process[12,31] and in order to prevent the hard breakdown of the devices, the saturation current of the transistor was set to approximately 1.5×10^{-5} A at V_{WL} = 1.5 V.[32,33]

In order to get insights into the impacts of the material properties of the HfO_2 thin films on the device performances, particularly on the endurance, two wafers including the 4kbit arrays of RRAM cells with HfO_2 films grown by AVD at temperatures of 320 and 400 °C, respectively, were investigated. It is worth to point out here that, all the measurements were carried out in pulse mode to examine the resistance state variability using pulses, because it is the operation mode used in the final high-end applications of RRAM device.

The Forming/Set/Reset operations on the arrays were performed by using an Incremental Pulse and Verify algorithm.[34] Reset operations were performed by applying the highest WL voltage available (2.8 V) to maximize the cells switching yield while avoiding the breakdown of the MIM cell. Pulses were applied during Forming by increasing V_{BL} with ΔV_{BL} = 0.01 V, whereas during Set and Reset ΔV_{BL} = 0.1 V and ΔV_{SL} = 0.1 V have been used, respectively. Each pulse featured duration of 10 μs, with a rise/fall time of 1 μs to avoid overshoot issues. Set operation was stopped on a cell when the read-verify current reached 20 μA, whereas Reset was stopped when 10 μA was reached. The program algorithm was also stopped at the pulse amplitude of 2.8 V, even when the read-out currents did not reach the threshold values. It is noted here that the set/reset voltages, which are defined as the critical voltages where the transition of HRS-LRS (set) or LRS-HRS (reset) starts, are smaller than the stop voltage of 2.8 V. Set and Reset BL/SL voltages necessary to reach the requested read-verify current targets are extracted from the characterization data and labeled as V_{SET} and V_{RES}, respectively.

The switching characteristics of both arrays were examined in detail. Here, typical $I-V$ sweep curves in dc mode, representing 100 different 1T-1R cells, for both 320 and 400 °C devices are first given in Figure 2a. Both devices are characterized with the same gate voltage of 1.5 V for the set procedure and 2.8 V for the reset operation. The gate voltages during the set and reset operation also define the current compliances. The switching voltages (V_{SWTICH}) of both arrays as a function of switching cycles were plotted in Figure 2b and c. Evidently, the set (V_{SET}) and reset (V_{RESET}) voltages of 400 °C devices (red curves) are both much lower than those of 320 °C devices (blue curves). For 400 °C devices, V_{SET} (~1.0 V) is always smaller than V_{RESET} (~1.4 V) while V_{SET} and V_{RESET} of 320 °C devices are rather close (initially ~1.8 V and increase). More importantly, beyond 10^2 cycles, V_{RESET} of 320 °C-devices starts to increase slightly, whereas those of 400 °C devices remain very stable until 10^4 cycles. The endurances of both devices were shown in Figure 2d and e, by plotting the cumulative probability of the LRS and HRS current values after 1 and 10^4 cycles. The higher On/Off ratio of the 400 °C device is caused by the higher currents in the LRS, while the HRS values of the 320 and 400 °C devices are similar. After 10^4 cycles, the HRS of the 320 °C device is strongly degraded (see Figure 2d), while HRS of the 400 °C device is just slightly increased after 10^4 cycles. The LRS of both films are less affected by cycling (see Figure 2e). We note here that, it can be observed in Figure 2d and e that the LRS and HRS currents could be higher than the threshold currents used for set (20 μA) and reset (10 μA) operation, which is because of the utilization of incremental step pulse programming (ISPP) technique in the measurements. By applying the ISPP algorithms, fluctuations of the read-verify currents could appear. These read-verify current oscillations can be interpreted either as the charging of a trap close to the surface of the CF or the movement of an atom/defect in the filament.[33]

To understand the origin of the variation of the RS switching parameters and the improvement of endurance of arrays by increasing the depositing temperature of HfO_2, a systematic material characterization was performed on ~20 nm HfO_2 thin films grown at 320 and 400 °C on TiN/Si substrates under completely same growth conditions with the HfO_2 films in above-described integrated devices, i.e., in an AVD chamber by using liquid precursor of TEMAH.

The crystallinity of the films was examined macroscopically by GIXRD and microscopically by HRTEM. Figure 3 shows

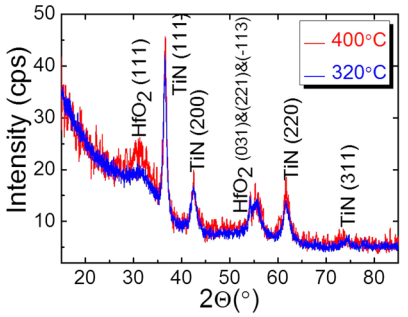

Figure 3. GIXRD measurements on HfO_2 films grown on TiN/Si (001) substrates at 320 °C (blue) and 400 °C (red) by AVD deposition.

the GIXRD 2Θ (15°−85°) results of the 320 °C film (blue) and the 400 °C film (red) performed at 1° angle of incidence around the TiN (200) Bragg reflection. It is noted that, GIXRD, compared to the normal specular 2Θ XRD measurements, provides a much higher sensitivity for detecting the possible nm-scale crystallites randomly distributed in a major amorphous film bulk. Figure 3 reveals that in both HfO_2 films, TiN peaks dominate in the XRD pattern, with the presence of TiN (111), TiN (200), TiN (220), and TiN (311) at 2Θ = 36.9°, 42.6°, 61.8° and 74.1°, respectively, which belong to the TiN with cubic structure. Besides, two main peaks with large widths are present corresponding to the HfO_2 with the monoclinic lattice. The diffraction peak located at 2Θ ~ 31.6° is related to the HfO_2 (111) reflection while the peak arise at 2Θ ~ 55.6°, is related to several monoclinic HfO_2 reflections close to each other including (031), (221), and (−113), which should theoretically appear at 2θ = 55.6°, 55.0°, and 55.8°, respectively. Moreover, the HfO_2 (111) peak intensity of the 400 °C sample is stronger than that of the 320 °C sample. These observations indicate that nanocrystallites appear in both HfO_2 samples and the density is relatively higher in the 400 °C sample. In other words, the deposition temperature of 320 °C already induces the crystallization of HfO_2 and higher temperatures lead to more and bigger crystallites.

The crystallinity of HfO_2 films was further examined microscopically by HRTEM and the results are shown in Figure 4. Figure 4a and b displays cross-sectional HRTEM images of HfO_2/TiN/Si samples deposited at 320 and 400 °C respectively. First, it can be seen that the TiN shows majorly a columnar feature demonstrating its polycrystalline nature, as detected by GIXRD. The film thicknesses of HfO_2 films are

DOI: 10.1021/acs.jpcc.6b12771
J. Phys. Chem. C XXXX, XXX, XXX−XXX

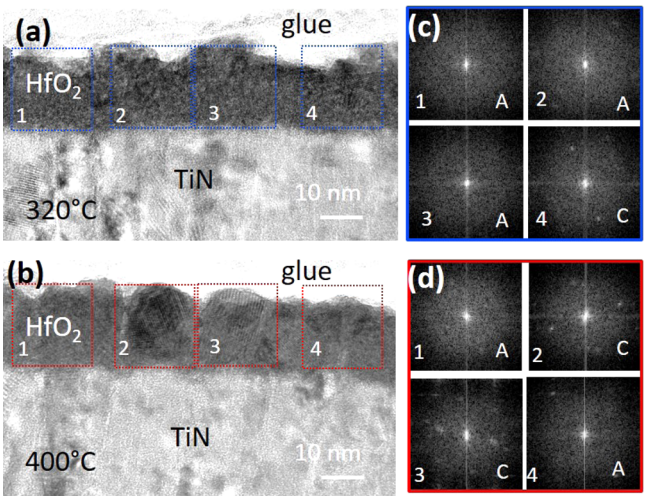

Figure 4. HRTEM images of the AVD HfO_2 films grown at (a) 320 °C and (b) 400 °C; (c) and (d) show FFT patterns of the regions denoted by 1, 2, 3, and 4 in (a) and (b), respectively. FFT patterns showing no spot is related to amorphous part and marked by "A"; FFT patterns displaying spotty feature are related to crystalline part and marked by "C".

both ~20 nm. Striped regions in HfO_2 films can also be found, although a disordered feature (thus being amorphous) of both samples predominates. This corroborates the presence of nanocrystallites in both mostly amorphous HfO_2 samples. Further details were revealed by performing fast Fourier transformation (FFT) treatment on different regions randomly selected and marked by 1, 2, 3, and 4 in (a) and (b), as shown in (c) and (d), respectively. In Figure 4c, displaying FFT patterns of the 320 °C sample, regions 1, 2, and 3 reveal a halo diffuse feature without any spot, indicating that they remain amorphous (thus being marked by "A" in the patterns). The pattern of region 4 shows clearly a spotty feature suggesting the crystalline characteristic of this part (thus being marked by "C"). Figure 4d shows FFT patterns of the 400 °C sample, in which region 1 and 4 also remain amorphous suggested by the halo diffuse feature, whereas regions 2 and 3 show evidently strong spotty feature revealing that nanocrystallites existing in these regions. Furthermore, compared to the region 4 of the 320 °C sample, more spots appear in regions 2 and 3 of the 400 °C sample, which indicates that more crystallites appear and the crystallite sizes augment with increasing deposition temperature. It is noted here that the observed spots are all related to the diffraction spots of the monoclinic HfO_2 lattice. These results well corroborate the GIXRD investigations.

It is known that the polycrystalline grain boundaries having oxygen deficient nature could serve as favorable conductive paths,[35,36] which could impact the RS properties of HfO_2 RRAM devices. However, in our case, both samples contain nanocrystallites and statistic studies on the forming process for both sample show the same forming voltage range and rather similar behavior (Supporting Information). Compared to 320 °C devices (Figure 2b and d), lower Set/Reset voltages, higher LRS currents and the slight difference of HRS of first cycle of 400 °C devices (Figure 2c and e) could possibly be induced by its higher density of nanocrystallites, which results in more grain boundaries thus more potential pathways of filaments. Nevertheless, it is difficult to correlate the lower RS voltages and better endurance of the 400 °C devices to the higher crystallite density. Particularly for the endurance, which is related to the hard breakdown of the oxide film, there is no clear proof that more grain boundaries would lead to a better endurance. The oxygen stoichiometry in HfO_2 films is another possible factor which could possibly influence the performance of RRAM devices. For example, Sharath et al.[37,38] reported that oxygen deficient HfO_{2-x} with intentional introduction of oxygen vacancies prepared by reactive molecular beam epitaxy (RMBE) could lead to smaller forming voltages of single HfO_2-MIM devices. In our results, both devices show rather same forming voltages (Figure S1 in the Supporting Information). Furthermore, AVD deposition is a good method to realize stoichiometric HfO_2 films therefore we believe the oxygen stoichiometry in both films in this study prepared under almost same procedures are rather similar.[39] On the other hand, solid theoretical and experimental results have been reported to clarify that the inevitable residual impurities like carbon originating from the incomplete decomposition and/or reaction of precursors (e.g., TEMAH) during the AVD or atomic layer deposition (ALD) process significantly impact the electrical properties of HfO_2 and high C concentration leads to easier hard breakdown of MOS or MIM devices.[16−19]

The carbon residues concentration was therefore investigated by Tof-SIMS, which offers a highly sensitive element detection up to 10^{18} atoms/cm^3 (~10 ppm) range. Figure 5 displays the

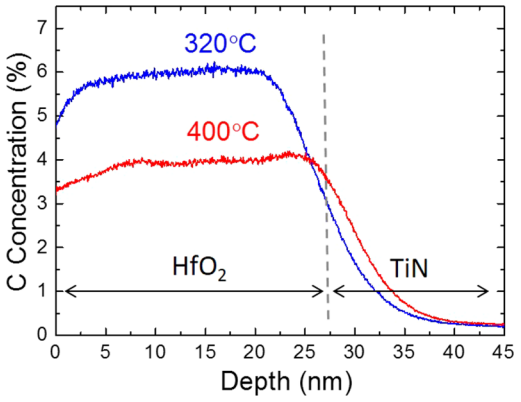

Figure 5. Tof-SIMS measurements revealing the relative atomic concentration of residual carbon in HfO_2 films deposited at 320 °C (blue, ~6%) and 400 °C (red, ~4%) as a function of the detecting depth.

Tof-SIMS results for carbon residues in AVD HfO_2 films as a function of the film depth. It is noted here that the absolute atomic concentration values were estimated by employing sputtering XPS measurements (Supporting Information). It was found that the 320 °C (blue) and 400 °C (red) HfO_2 films (from 0 to ~20 nm) possess average residual carbon concentration of ~6% and ~4%, respectively. When the detection depth is larger than 20 nm, i.e., when reaching the TiN layer, C concentration decreases rapidly to almost zero. The origin of the carbon residues is the $Hf[N(CH_3)(C_2H_5)]_4$ (TEMAH) precursor molecule, containing 12 carbon atoms per hafnium atom[16] and a higher deposition temperature leads to more complete precursor decomposition and reaction with oxidants thus lower residual C concentration. It is worth noting here that a further increase of the deposition temperature up to 450 °C could, on one hand, yield an even lower C residue concentration of ~2% (Supporting Information) and, on the other hand, still cannot completely remove carbon atoms and is

DOI: 10.1021/acs.jpcc.6b12771
J. Phys. Chem. C XXXX, XXX, XXX−XXX

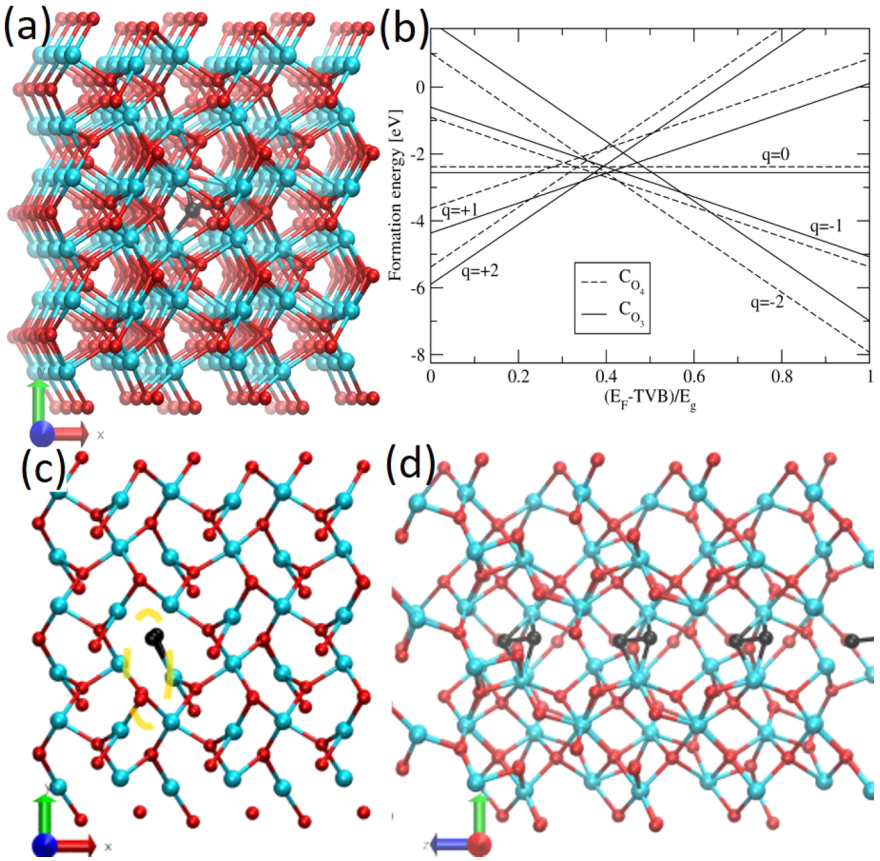

Figure 6. (a) Stick-and-ball structure of the relaxed C@O_3 substitutional with q = +2. Blue/red/black balls represent Hf/O/C atoms, respectively. (b) Formation energies for the incorporation of a remote C interstitial into a pre-existing $V_O^{\cdot\cdot}$ at a 3-/4-fold coordinated site, for different charge states. The describing reaction is $(HfO_2)_n + V@O_4 + C_i \rightarrow Hf_nO_{2n-1} + C@O_4$. TVB denotes the top of the valence band while $(E_F - TVB)/E_g$ from 0 to 1 represents the variation of the Fermi level position inside the bandgap from TVB to the bottom of the conduction band. (c) Top and (d) side views of a column of C atoms completely substituting a column of 4-coordinated O atoms.

incompatible with the fabrication process of 4kbit array 1T1R devices requiring a processing temperature limit of 400 °C.

The experimental investigations point out that different carbon residue concentrations in different RRAM cells are probably the reason responsible for the different devices performances, particularly the endurance. It is therefore of great interest and necessity to understand the role played by the carbon impurities during the RS. There have been several theoretical works studying the carbon defects positions[16,17] and their contribution to the "hard" breakdown of dielectric films.[20] However, to our knowledge, few systematic studies have been reported on the carbon defect effects on RS properties of HfO_2. We employ here the ab initio DFT method to explore this topic.

In HfO_2-based RRAM cells, the initial forming process yields a CF consisting of $V_O^{\cdot\cdot}$ as well as a large amount of $V_O^{\cdot\cdot}$ in the film bulk particularly close to the reservoir Ti layer.[40,41] Therefore, the first task is to understand the configuration of C impurities in HfO_2 film with such $V_O^{\cdot\cdot}$-rich environment. Calculations of total internal energies of C atoms in a variety of relevant configurations inside a monoclinic HfO_2 crystal were made within DFT, as implemented in the SIESTA package.[42] More calculation details, particularly for charged impurities, can be found in the Experimental Section.

In an oxygen deficient HfO_2 film, $V_O^{\cdot\cdot}$ can appear at 3-fold (O_3) and 4-fold (O_4) coordinated sites, with formation of the neutral vacancy at the O_4 site (V_{O4}^0) being 0.02 eV more favorable than having the neutral vacancy form at the O_3 site (V_{O3}^0).[43] On the other hand, when electron release to a Fermi level externally set close to the HfO_2 valence band edge is accounted for, the vacancy at the O_3 site is now favored with respect to the V_{O4}.[27,44] In particular, we obtain a charged vacancy formation energy difference between the V_{O3}^{+2} and V_{O4}^{+2} states of 0.7 eV, in agreement with the 0.76 eV obtained by Foster et al.[43]

Prior reports[17,18,20] pointed out that C impurities could exist at either an interstitial or a substitutional position. In the stoichiometric HfO_2, C atoms energetically prefer to stay at an interstitial position rather than substituting an oxygen atom.[20] Nevertheless, having pre-existing oxygen vacancies can significantly alter the structural preferences. We find that when a remote carbon interstitial fills an oxygen vacancy at an O_3 (or O_4) site (see Figure 6a), 2.6 eV (or 2.4 eV) are released. Thus, this suggests that, in oxygen-poor samples, C impurities will energetically tend to diffuse into the $V_O^{\cdot\cdot}$ positions and prefer to be located at O_3 sites. Considering the high energies released by C filling in $V_O^{\cdot\cdot}$, C atoms will be quite stable at these positions. This preference remains when the C impurities are allowed to become doubly positively charged, while doubly negatively charged C_{O4} impurities have lower formation energy when the Fermi level lies closer to the host conduction band edge, as demonstrated in Figure 6b, which plots formation energies for the incorporation of a remote C interstitial with different charge states into a pre-existing $V_O^{\cdot\cdot}$ at a 3-/4-fold

DOI: 10.1021/acs.jpcc.6b12771
J. Phys. Chem. C XXXX, XXX, XXX−XXX

coordinated site as a function of the Fermi level position inside the bandgap ranging from from the top of the valence band (TVB, $(E_F - TVB)/E_g = 0$) to the bottom of the conduction band ($(E_F - TVB)/E_g = 1$).

The above-obtained conclusion is of great importance because it suggests that the residual carbon atoms tend to diffuse into and stay at the locations of $V_O^{\cdot\cdot}$, which form the CF being responsible for the RS of HfO_2-based RRAM devices. Therefore, the carbon residues will play a role in impacting the RS properties of the RRAM cells.

It can be naturally expected that when the residual carbon concentration is relatively elevated, there will be more and more carbon atoms filling into $V_O^{\cdot\cdot}$ positions along with the switching cycles. Therefore, it is of interest to understand whether C impurities could form filaments being conductive. For this purpose, we studied the band structure of C atoms filling a $V_O^{\cdot\cdot}$ filament at O_4 sites with varying separation since, opposite to the single substitutional, the (charge neutral) C@O_4 filaments are strongly preferred over C@O_3 filaments by 1.66 eV/(C atom). Figure 6c shows a top view of a column of C atoms completely substituting a column of 4-coordinated O atoms. Note that the O_4 filament inside the region mark by a yellow ellipse acquires some O_3 character, suggesting that charge transfer effects are taking place between the C filament and that column of oxygens. Figure 6d shows a side view of the same structure demonstrating the strong Peierls distortion undergone by the C atoms.

Figure 7 shows the evolution of the bands in a system initially with a C@O_4 vacancy filament as the filling of the vacancies by C atoms increases from a separation 4a_3 (a), 2a_3 (b), a_3 (c), to 0.5a_3 (d), with a_3 being the length of the c-axis of monoclinic HfO_2. The blue lines in Figure 7d display the band details for a system without C filling to the V_{O4} filament. Evidently, we see that the addition of C@O_4 always introduces a couple of extra levels/bands in the gap (being dispersive at small separations) which indicates that the filaments are capable of conduction. These results suggest that although the carbon diffusion into the $V_O^{\cdot\cdot}$ filament during RS changes the filament nature and band structure of HfO_2, it does not hinder the conduction pathway and thus will not break the RS.

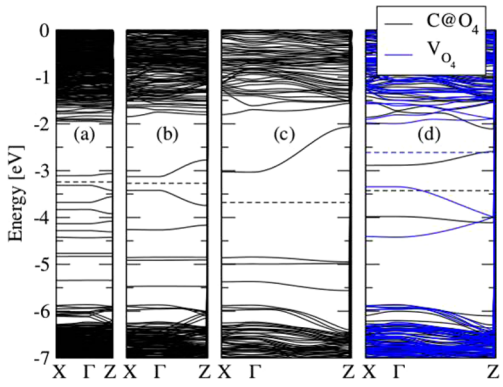

Figure 7. Evolution of the bands in a system initially with a V@O_4 vacancy filament [blue lines in (d)] as the filling of the oxygen vacancies by C atoms increases from a separation (a) 4a_3, to (b) 2a_3, to (c) a_3, to (d) 0.5a_3, with a_3 being the length of the c-axis of mHfO_2. Dashed lines represent Fermi levels.

In order to understand the difference between the original $V_O^{\cdot\cdot}$ CF and the C impurity CF, we studied their relative stability by computing the energy consumption to break the filaments. Figure 8a displays the final structure a neighboring oxygen atom to enter a vacancy filament (circled region) and the calculated total energy difference $E_{broken} - E_{unbroken}$ is 0.19 eV. Figure 8b depicts the final structure of a carbon atom (denoted by an arrow) leaving a C impurity filament (circled region) to a neighboring interstitial site and the total energy difference is much higher, 0.32 eV. This indicates that, for these two particular configurations, the C impurity filament is harder to be broken than the $V_O^{\cdot\cdot}$ filament.

Let us now consider the mechanism that carbon residues influence the RS properties of HfO_2, particulary the endurance by correlating our DFT calculations (Figures 6−8) and statistic electrical results (Figure 2). Initially residual carbon atoms exist with a homogeneous distribution in the film. The forming process induces the formation of $V_O^{\cdot\cdot}$ and CF and this oxgyen deficient environment in HfO_2 lead to the filling of carbon atoms into $V_O^{\cdot\cdot}$ sites (preferentially at O_4 sites) rather than staying interstitially in the HfO_2 lattice. It is noted here that, considering the Joule heating in filament could likely lead to even higher temperatures, it is also possible that local phase transformations from HfO_x to HfC/HfCO occur in the filament region. The carbon atom substitutions in the initial $V_O^{\cdot\cdot}$ filament will not change its conductive feature but once the carbon filament is formed, breaking it requires much higher energy (0.32 eV) compared to breaking the initial $V_O^{\cdot\cdot}$ filament (0.19 eV). The difference in required energy for breaking the conductive filament is reflected in the increase of reset voltages in the 320 °C devices, containing the higher residual carbon concentration of ∼6%. In addition, the HRS state is strongly impacted by cycling. The mean value as well as the dispersion of the HRS currents are increasing with the number of cycles, as illustrated in Figure 2d. Therefore, the window between LRS and HRS is closing much earlier in carbon rich HfO_2 devices compared to carbon reduced HfO_2 RRAM devices. These indicate that when the carbon-rich CF is formed, the RRAM cells become leakier and the HRS current continues increasing even with higher reset voltages, until the cells reach hard breakdown. This fact could be explained by the change of barrier height in the OFF state according to the quantum point contact (QPC).[21,45] Moreover, it should be also noted here that although the formation/rupture of the CFs is the RS mechanism in HfO_2-RRAM cells and our model explains well the observed electrical characteristics, the possible metal/oxide interface effect should not be completely ignored.[11,46] For instance, the possible carbon segregation around the electrode could partly contribute to the increase of the reset voltage and the increase of the HRS current during the cycles in 320 °C devices. Finally, it is also interesting to note here that, while carbon plays a negative role on RS properties of solid state HfO_2-based RRAM devices, in some other alternative RRAM devices, e.g., organic memories, carbon-related filament could become the main RS mechanism.[47]

4. CONCLUSION

In conclusion, we demonstrate that carbon residues existing in HfO_2-based RRAM devices play a key role to determine the RS property particularly the programming characteristics. A combination of statistical electrical investigation and detailed material study of the integrated HfO_2-based RRAM devices reveals that devices with HfO_2 films containing less carbon residues possess smaller switching voltages and a better reliability after 10^4 programming cycles. By employing systematic theoretical DFT calculations, the mechanism of

DOI: 10.1021/acs.jpcc.6b12771
J. Phys. Chem. C XXXX, XXX, XXX−XXX

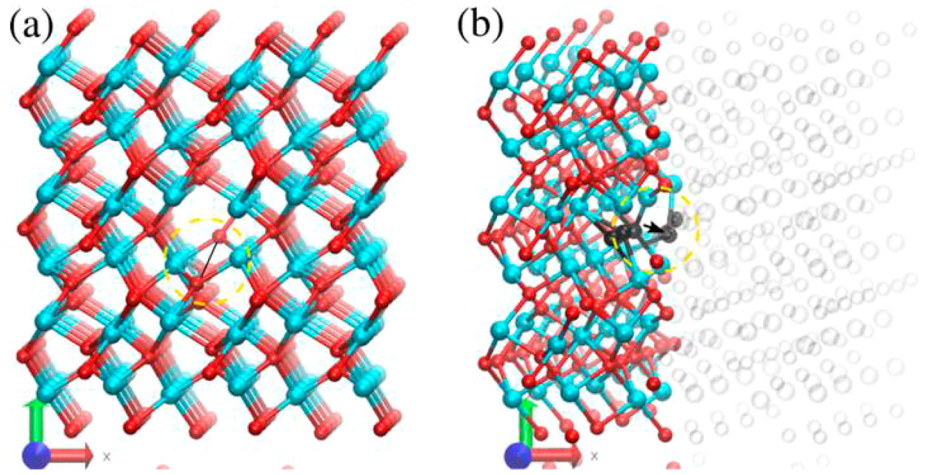

Figure 8. (a) Final structure of an oxygen atom entering a vacancy filament in order to break it. (b) Final structure of a carbon atom leaving a C impurity filament to a neighboring interstitial position in order to break it. Some balls representing atoms have been rendered transparent in order to facilitate the visualization of the path of the C atom.

the impact on RS of carbon atom via interaction with $V_O^{\cdot\cdot}$ filament was thoroughly understood. The carbon atoms prefer to diffuse into $V_O^{\cdot\cdot}$ sites and could also participate in forming conductive filaments. However, the higher energy required to break C filaments leads to the higher power consumption and the inferior endurance of the devices with 6% carbon residues. By reducing the residual carbon concentration to 4% by increasing the deposition temperature of HfO_2, highly reliable RRAM devices (up to 10^4 cycles) have been realized. Such in-depth materials and physics studies combined with the statistical studies on integrated 1T1R 4 kbit RRAM array not only deepen the understanding of the RS mechanism but also pave the way to achieve nonvolatile RRAM devices with lower power consumption and higher reliability.

■ ASSOCIATED CONTENT

Supporting Information

The Supporting Information is available free of charge on the ACS Publications website at DOI: 10.1021/acs.jpcc.6b12771.

Cumulative probability of forming voltages of both 320 and 400 °C 4kbit array devices; chemical depth profiling of different elements including residual carbon in the TiOx/HfO_2/TiN stack characterized by sputtering X-ray photoemission spectroscopy (XPS); Tof-SIMS measurements revealing the relative atomic concentration of residual carbon in HfO_2 films deposited at 320, 400, and 450 °C as a function of the detecting depth (PDF)

■ AUTHOR INFORMATION

Corresponding Authors

*(G.N.) E-mail: gangniu@mail.xjtu.edu.cn.
*(C.W.) E-mail: wenger@ihp-microelectronics.com.

ORCID

Gang Niu: 0000-0002-8813-8885

Author Contributions

G.N., X.C., T.S., and C.W. designed the work and wrote the manuscript. X.C. carried out the DFT calculations with the support of G.N. A.G., C.Z., P.O., and E.P. performed the statistic electrical measurements on 4kbit memory arrays. M.A.S. performed the HRTEM, and G.N. made related analysis. P.Z. made the GIXRD studies. G.N. and I.C. carried out XPS and Tof-SIMS studies. The manuscript was written through contributions of all authors. All authors have given approval to the final version of the manuscript.

Notes

The authors declare no competing financial interest.

■ ACKNOWLEDGMENTS

This work was supported by the ENIAC "PANACHE" project, the Spanish MINECO project No. TEC2015-67462-C2-1-R (MINECO/FEDER) and Deutsche Forschungsgemeinschaft (DFG) RRAM project SCHR 1123/7-1. The work was also partly supported by the Natural Science Foundation of China (Grant No. 51602247). The authors acknowledge Dr. Mindaugas Lukosius for the help on the HfO_2 and TiN films preparation and Dr. Karol Fröhlich for useful discussions.

■ REFERENCES

(1) Jiang, A. Q.; Wang, C.; Jin, K. J.; Liu, X. B.; Scott, J. F.; Hwang, C. S.; Tang, T. A.; Lu, H. B.; Yang, G. Z. A Resistive Memory in Semiconducting $BiFeO_3$ Thin-Film Capacitors. *Adv. Mater.* **2011**, *23*, 1277−1281.

(2) Jeong, D. S.; Thomas, R.; Katiyar, R. S.; Scott, J. F.; Kohlstedt, H.; Petraru, A.; Hwang, C. S. Emerging Memories: Resistive Switching Mechanisms and Current Status. *Rep. Prog. Phys.* **2012**, *75*, 076502.

(3) Sharma, Y.; Pavunny, S. P.; Fachini, E.; Scott, J. F.; Katiyar, R. S. Nonpolar Resistive Memory Switching with All Four Possible Resistive Switching Modes in Amorphous $LaHoO_3$ Thin Films. *J. Appl. Phys.* **2015**, *118*, 094506.

(4) Sharma, Y.; Pavunny, S. P.; Scott, J. F.; Katiyar, R. S. Non-Volatile Resistive Memory Switching in Pulsed Laser Deposited Rare-Earth Gallate-$GdGaO_3$ Thin Films. *ECS Trans.* **2015**, *66*, 287−293.

(5) Katiyar, R. K.; Misra, P.; Sharma, G. L.; Morell, G.; Scott, J. F.; Katiyar, R. S. Unipolar Resistive Switching and Associated Photoresponse in Sm doped $BiFeO_3$ Thin Film Grown by RF Sputtering. *MRS Online Proc. Libr.* **2013**, DOI: 10.1557/opl.2013.702.

(6) Khurana, G.; Misra, P.; Kumar, N.; Kooriyattil, S.; Scott, J. F.; Katiyar, R. S. Enhanced Resistive Switching in Forming-Free Graphene Oxide Films Embedded with Gold Nanoparticles Deposited by Electrophoresis. *Nanotechnology* **2016**, *27*, 015702.

(7) Mistry, K.; Allen, C.; Auth, C.; Beattie, B.; Bergstrom, D.; Bost, M.; Brazier, M.; Buehler, M.; Cappellani, A.; Chau, R.; et al. A 45nm Logic Technology with High-k+Metal Gate Transistors, Strained Silicon, 9 Cu Interconnect Layers, 193nm Dry Patterning, and 100% Pb-free Packaging. *IEEE Int. Electron Devices Meet.* **2007**, 247−250.

DOI: 10.1021/acs.jpcc.6b12771
J. Phys. Chem. C XXXX, XXX, XXX−XXX

(8) Waser, R.; Aono, M. Nanoionics-based Resistive Switching Memories. *Nat. Mater.* **2007**, *6*, 833−840.
(9) Chen, Y. Y.; Goux, L.; Clima, S.; Govoreanu, B.; Degraeve, R.; Kar, G. S.; Fantini, A.; Groeseneken, G.; Wouters, D. J.; Jurczak, M. Endurance/Retention Trade-off on HfO_2/Metal Cap 1T1R Bipolar RRAM. *IEEE Trans. Electron Devices* **2013**, *60*, 1114−1121.
(10) Govoreanu, B.; Kar, G. S.; Chen, Y.; Paraschiv, V.; Kubicek, S.; Fantini, A.; Radu, I. P.; Goux, L.; Clima, S.; Degraeve, R. $10 \times 10nm^2$ Hf/HfO_x Crossbar Resistive RAM with Excellent Performance, Reliability and Low-energy Operation. *IEEE Int. Electron Devices Meet.* **2011**, 31.6.1−31.6.4.
(11) Sawa, A. Resistive Switching in Transition Metal Oxides. *Mater. Today* **2008**, *11*, 28−36.
(12) Lorenzi, P.; Rao, R.; Irrera, F. Forming Kinetics in HfO_2-Based RRAM Cells. *IEEE Trans. Electron Devices* **2013**, *60*, 438−443.
(13) Brivio, S.; Tallarida, G.; Cianci, E.; Spiga, S. Formation and Disruption of Conductive Filaments in A HfO_2/TiN Structure. *Nanotechnology* **2014**, *25*, 385705.
(14) Huang, C.-Y.; Jieng, J.-H.; Jang, W.-Y.; Lin, C.-H.; Tseng, T.-Y. Improved Resistive Switching Characteristics by Al_2O_3 Layers Inclusion in HfO_2-Based RRAM Devices. *ECS Solid State Lett.* **2013**, *2*, P63−P65.
(15) Mok, I.-S.; Kim, J.; Lee, K.; Kim, Y.; Sohn, H.; Kim, H. Effect of Crystallinity on the Resistive Switching Behavior of $HfAlO_x$ Films. *J. Korean Phys. Soc.* **2014**, *64*, 419−423.
(16) Cho, M.; Jeong, D. S.; Park, J.; Park, H. B.; Lee, S. W.; Park, T. J.; Hwang, C. S.; Jang, G. H.; Jeong, J. Comparison Between Atomic-Layer-Deposited HfO_2 Films Using O_3 or H_2O Oxidant and $Hf[N(CH_3)_2]_4$ Precursor. *Appl. Phys. Lett.* **2004**, *85*, 5953−5955.
(17) Cho, M.; Kim, J. H.; Hwang, C. S.; Ahn, H.-S.; Han, S.; Won, J. Y. Effects of Carbon Residue in Atomic Layer Deposited HfO_2 Films on Their Time-Dependent Dielectric Breakdown Reliability. *Appl. Phys. Lett.* **2007**, *90*, 182907.
(18) Miao, B.; Mahapatra, R.; Wright, N.; Horsfall, A. The role of Carbon Contamination in Voltage Linearity and Leakage Current in High-k Metal-Insulator-Metal Capacitors. *J. Appl. Phys.* **2008**, *104*, 054510.
(19) Sowinska, M.; Bertaud, T.; Walczyk, D.; Thiess, S.; Calka, P.; Alff, L.; Walczyk, C.; Schroeder, T. In-operando Hard X-ray Photoelectron Spectroscopy Study on the Impact of Current Compliance and Switching Cycles on Oxygen and Carbon Defects in Resistive Switching Ti/HfO_2/TiN Cells. *J. Appl. Phys.* **2014**, *115*, 204509.
(20) Choi, M.; Lyons, J. L.; Janotti, A.; Van de Walle, C. G. Impact of Carbon and Nitrogen Impurities in High-κ Dielectrics on Metal-Oxide-Semiconductor Devices. *Appl. Phys. Lett.* **2013**, *102*, 142902.
(21) Niu, G.; Kim, H.-D.; Roelofs, R.; Perez, E.; Schubert, M. A.; Zaumseil, P.; Costina, I.; Wenger, C. Material Insights of HfO_2-Based Integrated 1-Transistor-1-Resistor Resistive Random Access Memory Devices Processed by Batch Atomic Layer Deposition. *Sci. Rep.* **2016**, *6*, 28155.
(22) Dingemans, G.; Jongbloed, B.; Knaepen, W.; Pierreux, D.; Jdira, L.; Terhorst, H. Merits of Batch ALD. *ECS Trans.* **2014**, *64*, 35−49.
(23) Lukosius, M.; Wenger, C.; Pasko, S.; Müssig, H.-J.; Seitzinger, B.; Lohe, C. Atomic Vapor Deposition of Titanium Nitride as Metal Electrodes for Gate-last CMOS and MIM Devices. *Chem. Vap. Deposition* **2008**, *14*, 123−128.
(24) Perdew, J. P.; Burke, K.; Ernzerhof, M. Generalized Gradient Approximation Made Simple. *Phys. Rev. Lett.* **1996**, *77*, 3865−3868.
(25) Zhao, X.; Vanderbilt, D. First-principles Study of Structural, Vibrational, and Lattice Dielectric Properties of Hafnium Oxide. *Phys. Rev. B: Condens. Matter Mater. Phys.* **2002**, *65*, 233106.
(26) Monkhorst, H. J.; Pack, J. D. Special Points for Brillouin-zone Integrations. *Phys. Rev. B* **1976**, *13*, 5188−5192.
(27) Leslie, M.; Gillan, N. J. The Energy and Elastic Dipole Tensor of Defects in Ionic Crystals Calculated by the Supercell Method. *J. Phys. C: Solid State Phys.* **1985**, *18*, 973.
(28) Makov, G.; Payne, M. C. Periodic Boundary Conditions in Ab initio Calculations. *Phys. Rev. B: Condens. Matter Mater. Phys.* **1995**, *51*, 4014−4022.
(29) Rurali, R.; Cartoixà, X. Theory of Defects in One-Dimensional Systems: Application to Al-Catalyzed Si Nanowires. *Nano Lett.* **2009**, *9*, 975−979.
(30) Sheu, S. S.; Chang, M. F.; Lin, K. F.; Wu, C. W.; Chen, Y. S.; Chiu, P. F.; Kuo, C. C.; Yang, Y. S.; Chiang, P. C.; Lin, W. P.; et al. A 4Mb Embedded SLC Resistive-RAM Macro with 7.2ns Read-write Random-Access Time and 160ns MLC-Access Capability. *ISSCC* **2011**, 200−202.
(31) Menzel, S.; Böttger, U.; Wimmer, M.; Salinga, M. Physics of the Switching Kinetics in Resistive Memories. *Adv. Funct. Mater.* **2015**, *25*, 6306−6325.
(32) Grossi, A.; Walczyk, D.; Zambelli, C.; Miranda, E.; Olivo, P.; Stikanov, V.; Feriani, A.; Suñé, J.; Schoof, G.; Kraemer, R.; et al. Impact of Intercell and Intracell Variability on Forming and Switching Parameters in RRAM Arrays. *IEEE Trans. Electron Devices* **2015**, *62*, 2502−2509.
(33) Grossi, A.; Perez, E.; Zambelli, C.; Olivo, P.; Wenger, C. Performance and reliability comparison of 1T-1R RRAM arrays with amorphous and polycrystalline HfO_2. *Ultimate Integr. Silicon (EUROSOI-ULIS)* **2016**, 80−83.
(34) Grossi, A.; Zambelli, C.; Olivo, P.; Miranda, E.; Stikanov, V.; Walczyk, C.; Wenger, C. Electrical characterization and modeling of pulse-based forming techniques in RRAM arrays. *Solid-State Electron.* **2016**, *115*, 17−25.
(35) Lanza, M.; Zhang, K.; Porti, M.; Nafría, M.; Shen, Z. Y.; Liu, L. F.; Kang, J. F.; Gilmer, D.; Bersuker, G. Grain Boundaries as Preferential Sites for Resistive Switching in the HfO_2 Resistive Random Access Memory Structures. *Appl. Phys. Lett.* **2012**, *100*, 123508.
(36) Xue, K.-H.; Blaise, P.; Fonseca, L. R. C.; Molas, G.; Vianello, E.; Traoré, B.; De Salvo, B.; Ghibaudo, G.; Nishi, Y. Grain Boundary Composition and Conduction in HfO_2: An ab Initio Study. *Appl. Phys. Lett.* **2013**, *102*, 201908.
(37) Sharath, S. U.; Bertaud, T.; Kurian, J.; Hildebrandt, E.; Walczyk, C.; Calka, P.; Zaumseil, P.; Sowinska, M.; Walczyk, D.; Gloskovskii, A.; et al. Towards Forming-Free Resistive Switching in Oxygen Engineered HfO_{2-x}. *Appl. Phys. Lett.* **2014**, *104*, 063502.
(38) Sharath, S. U.; Kurian, J.; Komissinskiy, P.; Hildebrandt, E.; Bertaud, T.; Walczyk, C.; Calka, P.; Schroeder, T.; Alff, L. Thickness Independent Reduced Forming Voltage in Oxygen Engineered HfO_2 Based Resistive Switching Memories. *Appl. Phys. Lett.* **2014**, *105*, 073505.
(39) Lukosius, M.; Wenger, C.; Pasko, S.; Müssig, H.-J.; Seitzinger, B.; Lohe, C. Atomic Vapor Deposition of Titanium Nitride as Metal Electrodes for Gate-last CMOS and MIM Devices. *Chem. Vap. Deposition* **2008**, *14*, 123−128.
(40) Walczyk, C.; Wenger, C.; Walczyk, D.; Lukosius, M.; Costina, I.; Fraschke, M.; Dabrowski, J.; Fox, A.; Wolansky, D.; Thiess, S.; et al. On the Role of Ti Adlayers for Resistive Switching in HfO_2-Based Metal-Insulator-Metal Structures: Top Versus Bottom Electrode Integration. *J. Vac. Sci. Technol., B: Nanotechnol. Microelectron.: Mater., Process., Meas., Phenom.* **2011**, *29*, 01AD02.
(41) Kim, H.; McIntyre, P. C.; On Chui, C.; Saraswat, K. C.; Stemmer, S. Engineering Chemically Abrupt High-k Metal Oxide/Silicon Interfaces Using An Oxygen-Gettering Metal Overlayer. *J. Appl. Phys.* **2004**, *96*, 3467−3472.
(42) Soler, J. M.; Artacho, E.; Gale, J. D.; Garcia, A.; Junquera, J.; Ordejon, P.; Sanchez-Portal, D. The SIESTA Method for Ab initio Order- N Materials Simulation. *J. Phys.: Condens. Matter* **2002**, *14*, 2745.
(43) Foster, A. S.; Lopez Gejo, F.; Shluger, A. L.; Nieminen, R. M. Vacancy and Interstitial Defects in Hafnia. *Phys. Rev. B: Condens. Matter Mater. Phys.* **2002**, *65*, 174117.
(44) Broqvist, P.; Pasquarello, A. Oxygen Vacancy in Monoclinic HfO_2: A Consistent Interpretation of Trap Assisted Conduction,

DOI: 10.1021/acs.jpcc.6b12771
J. Phys. Chem. C XXXX, XXX, XXX−XXX

Direct Electron Injection, and Optical Absorption Experiments. *Appl. Phys. Lett.* **2006**, *89*, 262904.
(45) Miranda, E. A.; Walczyk, C.; Wenger, C.; Schroeder, T. Model for the Resistive Switching Effect in HfO_2 MIM Structures Based on the Transmission Properties of Narrow Constrictions. *IEEE Electron Device Lett.* **2010**, *31*, 609−611.
(46) Yoon, J.-W.; Yoon, J. H.; Lee, J.-H.; Hwang, C. S. Impedance Spectroscopic Analysis on Effects of Partial Oxidation of TiN Bottom Electrode and Microstructure of Amorphous and Crystalline HfO_2 Thin Films on Their Bipolar Resistive Switching. *Nanoscale* **2014**, *6*, 6668−6678.
(47) Lee, B.-H.; Bae, H.; Seong, H.; Lee, D.-I.; Park, H.; Choi, Y. J.; Im, S.-G.; Kim, S. O.; Choi, Y.-K. Direct Observation of a Carbon Filament in Water-Resistant Organic Memory. *ACS Nano* **2015**, *9*, 7306−7313.

DOI: 10.1021/acs.jpcc.6b12771
J. Phys. Chem. C XXXX, XXX, XXX−XXX